Temporal and Spectral Characteristics of Persistent Emission and Special Bursts of Magnetar SGR J1935+2154 Based on Insight-HXMT

Xue-Feng Lu[1,2] [iD], Li-Ming Song[1,2] [iD], Ming-Yu Ge[1], Shuang-Nan Zhang[1,2], Jin-Lu Qu[1], Ce Cai[3], Cong-Zhan Liu[1], Cheng-Kui Li[1], Yu-Cong Fu[4], and Ying-Chen Xu[1,2]

[1] Key Laboratory of Particle Astrophysics, Institute of High Energy Physics, Beijing 100049, China; songlm@ihep.ac.cn
[2] University of Chinese Academy of Sciences, Chinese Academy of Sciences, Beijing 100049, China
[3] College of Physics and Hebei Key Laboratory of Photophysics Research and Application, Hebei Normal University, Shijiazhuang 050024, China
[4] Department of Astronomy, Beijing Normal University, Beijing 100875, China

Abstract

In October 2022, the magnetar SGR J1935+2154 entered the active outburst state. During the episode, the Insight-HXMT satellite carried out a long observation that lasted for 20 days. More than 300 bursts were detected, and a certain amount of persistent radiation signals were also accumulated. This paper mainly introduces the results of persistent radiation profile folding and period search based on Insight-HXMT data. At the same time, the burst phase distribution characteristics, spectral lag results of burst, the spectral characteristics of zero-lag bursts and the time-resolved spectral evolution characteristics of high-flux bursts are reported. We found that there is no significant delay feature during different energy bands for the bursts of SGR J1935+2154. The observed zero-lag burst does not have a unique spectrum. The time-resolved spectrum of the individual burst has consistent spectral types and spectral parameters at different time periods of the burst. We also find that the burst number phase distribution and the burst photon phase distribution have the same tendency to concentrate in specific regions of the persistent emission profile.

Key words: radiation mechanisms: general – dense matter – magnetic fields

1. Introduction

Magnetars are a special class of celestial objects in the universe that possess super-strong magnetic fields (typically exceeding 10^{14} G). They are often thought of as young neutron stars. Compared to conventional pulsars, magnetars are characterized by intense energetic phenomena in X-ray band and soft gamma-ray band (Kaspi & Beloborodov 2017). This is why magnetars are commonly classified as anomalous X-ray pulsars and soft gamma repeaters (SGRs) (Woods et al. 2008; Scholz & Kaspi 2011). It is generally believed that magnetars are powered by the decay of their supercritical magnetic fields, perhaps either an external magnetic field (Kouveliotou et al. 1998) or an internal magnetic field (Thompson & Duncan 1995).

SGR J1935+2154 was discovered in 2014 when the Swift-BAT (Burst Alert Telescope) was triggered by a short burst from the Galactic plane (Stamatikos et al. 2014). Subsequent Chandra observations localized the burst in the direction of the supernova remnant G57.2+0.8 (Kothes et al. 2018). Based on data from Chandra and XMM-Newton, a 3.24 s spin period and a spin-down rate of $1.43(1) \times 10^{-11}$ s s^{-1} were found, indicating a surface dipolar magnetic field strength of approximately 2.2×10^{14} G (Israel et al. 2016). Combined with its burst characteristics, the source was identified as a magnetar. In

2015, 2016, 2019 and 2020 SGR J1935+2154 has many burst activity episodes, releasing a lot of energy in persistent and burst emission (Younes et al. 2017; Lin et al. 2020).

SGR J1935+2154 has been very active since the beginning of October 2022. Swift reported multiple bursts (Palm 2022) on October 10, Fermi observed an increasing trend of bursts (Roberts et al. 2022) on October 11 and 12, and then NICER began to observe the source starting at October 12 17:32:40 UTC for a total exposure time of 8.5 ks spanning 15.8 hr. During the observation, NICER detected a total number of 112 burst candidates. A preliminary result shows that the burst rate of 0.013 per second is a magnitude lower than the 2020 burst storm level recorded by NICER. NICER observation also find an increased persistent emission from the source, which can be best fitted with an absorbed blackbody plus a power-law model in the 1–8 keV. The best fit blackbody temperature is 0.70 ± 0.03 keV and the power law photon index is 1.0 ± 0.2. The unabsorbed 0.5–10 keV flux is an order of magnitude higher than quiescent flux level (Younes et al. 2020, 2022). Based on the NICER proposal, NuSTAR also performed an observation of the source from October 2022 14 02:00 UTC with an exposure totaling 50 ks. NuSTAR's observation covered the second burst forest time which begin on October 2022 14 at 19:21:47 UTC and ended on October 2022 14 19:10:00 UTC.

Over a hundred bursts were detected during this forest. Detailed analysis of the observation is ongoing (Enoto et al. 2022).

During these active episodes of SGR J1935+2154, two fast radio burst (FRB) events were detected. One occurred at October 2022 14 19:21:47 UTC, both CHIME (known as Canadian Hydrogen Intensity Mapping Experiment) (Dong & Chime/Frb Collaboration 2022) and GBT (known as Green Bank Telescope) (Maan et al. 2022) detected this signal. The coincident X-ray burst was reported by GECAM-B, GECAM-C (Wang et al. 2022) and Konus-Wind (Frederiks et al. 2022). Another FRB occurred at October 2022 21 10:01:45.84 UTC, only Yunnan 40 m radio telescope detected a radio burst at 2.245 GHz (Huang et al. 2022), a coincident single X-ray burst was detected by Insight-HXMT/HE (Li et al. 2022). No more detailed results have been reported. In Ge et al. (2024) the spin properties based NICER has been reported with $f = 0.3075277$ Hz and $f1 = -3.92 \times 10^{-12}$ Hz s^{-1} at $T_0 = 59865$ MJD. The spin evolution of SGR J1935+2154 is found to be steady around the time of the radio bursts 221 014 and 221 021.

From October 2022 13 04:51:38 UTC to 2022 November 1 15:48:26 UTC, Insight-HXMT executed a Target of Opportunity (ToO) observation of SGR J1935+2154 with a total exposure time 943.87 ks. A preliminary search yielded about 371 burst candidates. The observation of Insight-HXMT also caught the second burst forest period, during which many bursts are very dense and difficult to distinguish, thus affecting the final total number of bursts. In this paper, we mainly analyze the characteristics of the persistent emission and burst lag properties. Section 2 gives the HXMT data reduction methods, Section 3 describes the persistent emission and the burst phase characteristics, Section 4 gives the spectra lag characteristics and the energy spectrum characteristics of the zero lag bursts, the time decomposition spectrum characteristics and the burst characteristics with special spectral shapes. Section 5 gives the special burst wholes spectrum cannot be well fitted with either blackbody+blackbody (BB+BB) or cut off power law (CPL) models.

2. Observation and Data Reduction

Insight-HXMT was launched on 2017 June 15, which carries three collimated telescopes covering 1–10 keV (the Low Energy X-ray telescope, LE, geometrical area of 384 cm^2), 5–30 keV (the Medium Energy X-ray telescope, ME, geometrical area of 952 cm^2) and 20–250 keV (the High Energy X-ray telescope, HE, geometrical area of about 5000 cm^2) (Cao et al. 2020; Chen et al. 2020; Liu et al. 2020; Zhang et al. 2020).

During the outburst activity in October 2022, the Insight-HXMT satellite carried out a 20 day ToO observation of the magnetar SGR J1935+2154, spanning from October 13 to November 1, with a cumulative effective observation time of 1461 ks. The specific observation time list is shown in Table 1.

The 1L level observation data of Insight-HXMT were chosen for analysis, and the Insight-HXMT Data Analysis Software package (HXMTDAS) version 2.05 was utilized for preprocessing the data. Initially, *hepical*, *mepical* and *lepical* were utilized for event photons calibrate of HE, ME and LE, respectively, with Calibration Database (CALDB) of Insight-HXMT. Then good time interval was done directly for HE calibrated data with *hegtigen*. For LE data with the two-split events reconstruction and classification were executed with *lerecon* first and then *legtigen*. For ME data, *megrade* was used to calculate event grade and dead time correction before *megtigen*. Finally, *hescreen*, *mecreen* and *lescreen* were used to do good time data extraction and also *hxbary* was used to do solar system centroid correction for subsequent phase analysis. Using the screened data, a preliminary search for the burst was conducted via Cai ce, with specific methods referenced in Cai et al. (2022b). After the burst search authentication is completed, the data will be re-extracted based on the burst time information. Based on the refined burst data, further analysis is conducted using *hespec* to generate energy spectra, *hebkg* to generate background spectra, and *heresp* to generate response matrix files. Xspec 12.0 is employed to fit the burst spectrum. For spin period search, all the burst signals and spurious pulse signals are thoroughly removed.

3. Persistent Emission

For the persistent emission analysis, we employ the Insight-HXMT LE data which excluded any potential burst signals, and also the solar system barycenter correction was carried out before phase analysis. The ephemeris derived from NICER data with $f = 0.3075277$ Hz and $f1 = -3.92 \times 10^{-12}$ Hz s^{-1} (at $T_0 = 59865$ MJD) in Ge et al. (2024) were used to find the most significant LE data segment which can be used for phase analysis. Finally, the observation data segments 59871.0876 MJD to 59880.4756 MJD and 59882.33867 MJD to 59884.20446 MJD were found to exhibit significant persistent radiation signals within the energy range of 0.74–5.85 keV. A rotation period search of the magnetar in the combined data of two segments was performed, at the position of the maximum χ^2 value of 125.71 (corresponding to the largest $Z_1^2 = 125.287$, Z^2 is conceptually similar to the χ^2 but has high values when the signal is well described by a small number of sinusoidal harmonics, the specific expression can be found in Buccheri et al. 1983), we obtained the optimal rotation frequency with $f = 0.3076134(4)$ Hz. The number in parentheses represents the error in the last digit. The phase profile with different ephemeris is presented in Figure 1, and it is evident that the NICER and Insight self-search ephemeris produce highly similar results. However, due to statistical fluctuations,

Table 1
Insight-HXMT Observation Time List of SGR J1935+2154 in October 2022

Target	Start Time	End Time	Observation Time (ks)	Exposure Time (ks)
SGR J1935+2154	2022-10-13 04:51:38	2022-10-25 18:42:33	1086.665	725.883
SGR J1935+2154	2022-10-26 02:28:59	2022-10-27 16:44:06	137.707	81.898
SGR J1935+2154	2022-10-28 03:43:01	2022-10-28 16:33:33	46.232	27.05
SGR J1935+2154	2022-10-29 03:32:27	2022-10-29 16:23:01	46.234	26.859
SGR J1935+2154	2022-10-30 03:21:57	2022-10-30 17:47:49	51.952	29.298
SGR J1935+2154	2022-10-31 03:11:29	2022-10-31 16:02:03	46.234	26.57
SGR J1935+2154	2022-11-01 03:01:02	2022-11-01 15:48:26	46.044	26.312

Note. Observation time includes the time in SAA and Earth occlusion time.
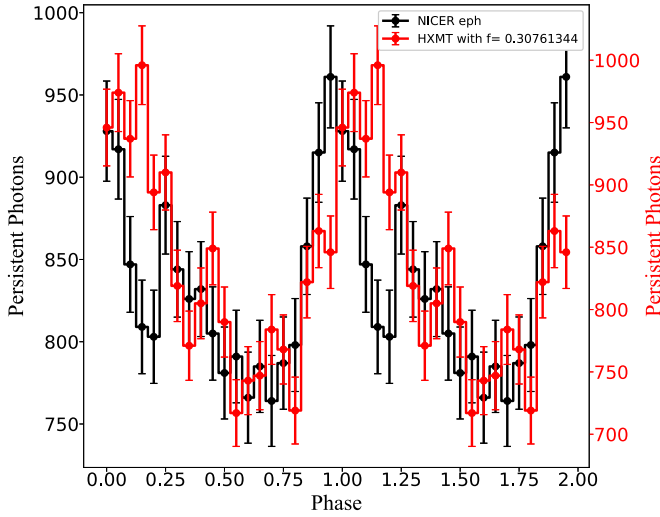

Figure 1. Comparing the persistent X-ray pulse profile with different ephemeris. The red line using the search period $f = 0.3076134$ Hz ($T_0 = 59865$ MJD), the black line using NICER ephemeris with $f = 0.3075277$ Hz and $f1 = -3.92 \times 10^{-12}$ Hz s^{-1} (at $T_0 = 59865$ MJD). The left axis is NICER ephemeris scale, and the right axis is the Insight-HXMT searched ephemeris scale. Both ephemeris use Insight-HXMT LE data in 0.75–5.85 keV.

Figure 2. The rising and falling time distribution of bursts during 2022 outburst episode. The left panel is the rising time statistic result and the log normal fitting result. The right panel is the result for burst falling time. The purple lines represent HE burst time, the blue lines represent ME burst time while the green lines represent LE time. Solid lines are the statistic result of the observed result, and dashed lines are the fitting result.

both ephemeris possess their own errors, which lead to certain differences in the profile derived from the two.

Based on the above high flux persistent emission period data, we also conducted a persistent spectrum analysis. Initially, we eliminated all bursts and other interference signals during the period. Subsequently, we utilized the standard instructions *lespec*, *lebkgmap*, and *leresp* of HXMT-HEADAS to generate the corresponding energy spectrum, background, and response matrix files. However, the results indicate that due to the higher background count compared to the source count in LE, we were unable to obtain a spectral result for persistent emission.

Due to the large margin of errors, here we just give a simple result of Insight-HXMT pulse period search. When we do burst phase analysis, the ephemeris data $f = 0.3075277$ Hz and $f1 = -3.92 \times 10^{-12}$ Hz s^{-1} (at $T_0 = 59865$ MJD) in Ge et al. (2024) were selected for a long time span.
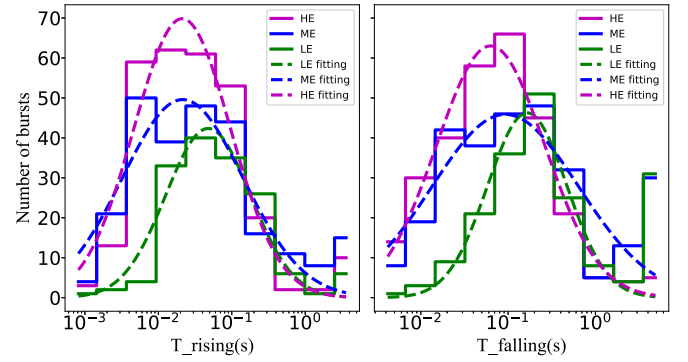
4. Burst Properties

4.1. Morphological Characteristics and Phase Distribution of the Bursts

The search and certification of bursts are consistent with the description in Cai et al. (2022b). First, we search for possible triggers based on significance. Then, we use the Bayesian blocks method described in Scargle et al. (2013) to further confirm the bursts and extract the start and end time information of the bursts. Based on the extracted burst time information, we first study the burst morphology. Since the bursts are dense in the burst forest time period, Bayesian blocks have difficulty accurately extracting the burst time information. Therefore, when conducting morphological analysis, only the remaining 295 bursts after excluding the burst forest were selected. We carried out statistical analyses on the rise and fall times of high, medium, and low-energy bursts, and fitted them using a lognormal distribution. The fitting results are presented in Figure 2. The fitted mean rise and fall times are summarized in Table 2. We compared the data of 75 bursts in 2020 April and found that on average, during the two burst periods, all

Table 2
Burst Rise and Fall Time for SGR J1935+2154 in 2020 and 2022 Outbursts

Telescope	Rising Time (ms)		Falling Time (ms)	
	2020	2022	2020	2022
HE	9.8	21	54.3	63
ME	4.2	16	42.6	66
LE	5.5	47	50.1	165

Figure 3. Comparing the persistent X-ray pulse profile and the burst photons arrival time and burst peak time phase distribution. The upper panel is burst photons phase distribution, and the lower panel is burst peak times phase distribution. The black curve is the persistent profile of SGR J1935+2154 obtained from NICER data, the blue curve is the HE burst photons phase distribution, while the red curve is the HE burst peak time phase distribution. All the data use the ephemeris $f = 0.3075277$ Hz and $f1 = -3.92 \times 10^{-12}$ Hz s^{-1} (at $T_0 = 59865$ MJD) from Ge et al. (2024).

energy bands showed a trend of fast rise and slow fall, which is consistent with the reported morphological characteristics of magnetar bursts in Scholz & Kaspi (2011).

Similar to the method described in Lu et al. (2023), we carried out statistical analysis on the phase distribution of photons within the burst and the phase distribution of the burst peak time. We found that the highest flux of burst photons occurred at the valley position where the continuous radiation sub-peak transitions to the main peak. During this outburst, we found that the burst peak time phase distribution has a consistent trend with the burst photons, as shown in Figure 3. At the phase with highest photon counts, the total number of bursts is also relatively large, and the number distribution of bursts has a similar trend to the phase profile which means more bursts sit at the phase peak position. Moreover, the χ^2 test shows that the phase distribution of the burst peak has a significance level greater than 3σ compared to a uniform distribution.

4.2. Time-lag of Burst Spectra

The time resolution of the HE telescope is less than 10 μs, the ME 255 μs, and the LE 980 μs. To achieve more precise lag time resolution, we opt to utilize data from HE and ME for time-lag analysis. We employ a basic light curve with a time resolution of 0.5 ms for cross-correlation analysis. For the calculation of time delays, we utilize the modified cross-correlation function method described in Li (2004), also referred to as the MCCF method. The definition of MCCF is as follows:

$$\text{MCCF}(k, \triangle t) = \frac{1}{M_{\triangle t}} \sum_{m=1}^{M_{\triangle t}} \sum_i u_m(i; \triangle t) v_{m+k}(i; \triangle t) / \sigma_u \sigma_v \quad (1)$$

$$u_m(i; \triangle t) = x_m(i; \triangle t) - b_{x_m}(i; \triangle t) \quad (2)$$

$$v_m(i; \triangle t) = y_m(i; \triangle t) - b_{y_m}(i; \triangle t) \quad (3)$$

$$\sigma_u^2 = \sum_i u_m(i; \triangle t)^2 \quad (4)$$

$$\sigma_v^2 = \sum_i v_m(i; \triangle t)^2. \quad (5)$$

In the formula, $x(j; \delta t)$ and $y(j; \delta t)$ are the basic light curves, and we use the light curve of 0.5 ms here according to the time
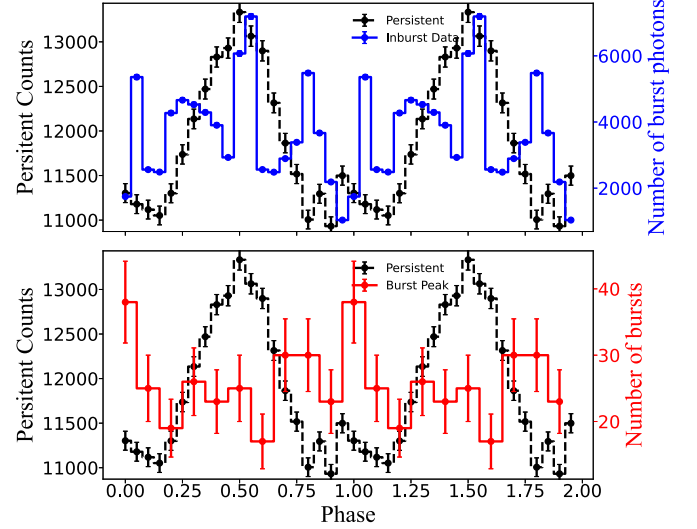
resolution of the Insight-HXMT instrument described before. $m = 1, 2...M_{\triangle t}$ is the phase factor, $u_m(\triangle t)$ and $v_m(\triangle t)$ are the original light curves of $x_m(\triangle t)$ and $y_m(\triangle t)$ after subtracting the background and rebin. $\triangle t = M_{\triangle t} \delta_t$, where $\triangle t$ is from 0.5 ms to 2.5 ms in this article, where b_{x_m} and b_{y_m} the background light curves corresponding to $x_m(\triangle t)$ and $y_m(\triangle t)$, respectively. The energy spectrum delay between the two light curves is $\tau(\triangle t) = k_{\max} \delta_t$.

Since the spectral lag analysis compares different energy bands of the same pulse signal, the maximum delay usually does not exceed half of the pulse width. As mentioned earlier, the typical pulse widths of HE and ME are 100 ms. Therefore, in this study, we set the maximum delay limit to -60 and 60 ms to exclude the large statistical errors caused by weak bursts. During analysis, we found the high-flux bright bursts usually have a lag time of a few milliseconds order, which also reflects the assumption is very reasonable. It is worth noting that this assumption does not affect the research results in this paper, as we also excluded bursts with large delay errors during statistical analysis.

The Monte Carlo sampling technique is employed to assess the uncertainty associated with spectral lag. By utilizing this approach, we generated 1000 samples from the original light curve and obtained the MCCF lag times of these samples. To obtain average delay information and sigma values, we employed statistical analysis of the sample lag times and fitted the statistical data with the Gaussian function. Based on the
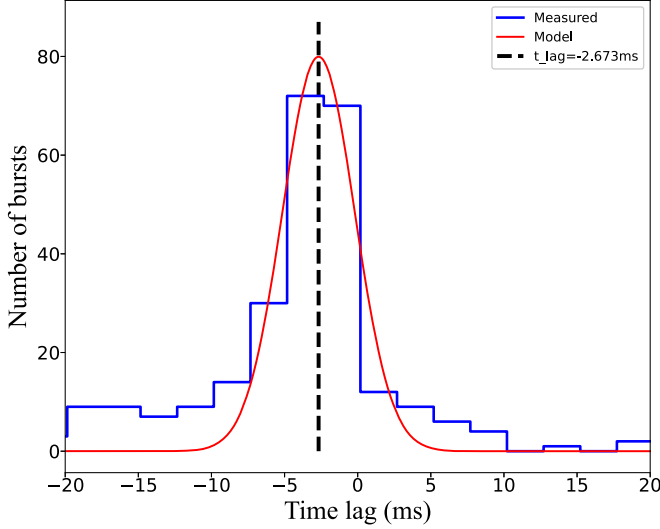
Figure 4. Time lag statistic result for 10–20 keV vs. 60–100 keV. The blue line is the histogram result for burst MCCF lags, the red line is the Gaussian fitting model. The black dashed line is the expected value of the fitting model.

Table 3
Time Lag between Different Energy Bands

Energy Band (keV)	t_{lag} (ms)	t_{sigma} (ms)	ts_{lag} (ms)	ts_{sigma} (ms)
10–30 versus 30 more	−0.951	2.236	−2.673	2.472
10–20 versus 60–100	−2.135	4.065	−4.383	4.068

previous assumptions, when performing statistical analysis on MCCF lags, we selected bursts with lag time amplitude less than 60 ms and fitting sigma less than 20 ms for analyzing, the same rule used in Xiao et al. (2023). We analyzed the spectral lag distribution of photons with energy 10–30 keV to more than 30 keV, and the spectral lag distribution of photons with energy 10–20 to 60–100 keV. The results are shown in Figure 4 and Table 3. The t_{lag} represents the statistical analysis result of the delay time obtained by directly performing MCCF on the two observation energy bands of the burst. The t_{sigma} represents the sigma of the Gaussian function after statistics of the MCCF delay. The ts_{lag} and ts_{sigma} represent the Monte Carlo sampling lag statistical results. It can be seen from the analysis results that there is no obvious delay in the statistical sense between high and low energy photons. In other words, the high-energy and low-energy spectra actually do not have significant delay characteristics and arrive at the detection equipment almost at the same time.

4.3. Spectra Properties of Zero-lag Burst

During the delay analysis, we found that there is no significant lag characteristic between photons in different energy bands. In order to further understand the characteristics of this non-delay burst, we specially selected bursts whose delay results calculated by MCCF were in the range of −0.5 to 0.5 ms, and performed fitting analysis on the energy spectra of these bursts. The spectral analysis results are shown in Table 4. We have not found that the energy spectra of these bursts have specific spectral types. Similar to the result in Cai et al. (2022a) for the 2020 outburst, most of the energy spectra of these bursts

can be fitted using BB+BB model. The low temperature of the double blackbodies is about 2.2 keV, and the high temperature is about 12 keV, a small number of bursts can be fitted by CPL, with a spectral index less than 1 and a cutoff energy less than 30 keV.

Because there is no specificity in the energy spectrum of zero-lag bursts, we further studied the time-resolved spectra of high-flux bursts in these zero-lag bursts to observe whether there are evolutionary characteristics of the energy spectrum in different time periods of a burst. We have no specific restrictions on the time division of a burst. For single-peak burst, we cut at the peak point to ensure that there are sufficient photons in the two periods before and after. While for bursts with multiple peaks, we separate them at the valley point between two strong peaks to ensure sufficient statistics before and after as shown in Figure 5. The fitting parameters of the decomposition spectrum are shown in Table 4 and Figure 6. We found that the rising and falling periods of a burst's energy spectrum maintain the same spectral type, and there is no significant difference in the spectral parameters. The temperature of the BB+BB spectrum and the power exponent and cutoff energy of the CPL remain highly consistent in any segment, which shows that the two temperatures of the double blackbody cannot come from the same plane region but from a three-dimensional space. It is worth noting that while fitting the burst energy spectrum, the model selection of the energy spectrum is not unique. In fact, these bursts exhibit more or less the same energy spectrum characteristics as the special burst discussed in Section 5, i.e., low-energy blackbody and high-energy cut off power-law characteristics. However, due to insufficient statistical data on the bursts themselves, not every burst can be quantitatively characterized with significant spectral features for model selection. When selecting the energy spectrum, we not only consider the Bayesian Information Criterion (BIC) but also take into account the residual structure and spectral parameter error of the fit. We choose the model with the smallest residual structure and spectral parameter error when the BIC values are similar.

4.4. Bursts with Special Spectral Models

When studying the decomposition spectra of bursts, we expanded the sample numbers and selected some bi-peaks and multi-peaks bursts whose MCCF lag was not 0 but had enough photons to ensure statistics before and after segmentation. In

Table 4
The Time-resolved Spectral Parameters of Bursts with BB+BB Spectral

Type	ID	Burst_start	Burst_stop	T_{bb}	t_lag	ts_lag	σ	KT_low	KT_high	Cstat/dof
Total burst[a]	0	340260979.802	340260980.117	0.315	−1.0	−1.46	−0.89	$2.12^{+0.15}_{-0.13}$	$12.2^{+0.51}_{-0.48}$	89.2/78.0
	1	340266063.664	340266064.1	0.436	0.0	−0.6	1.59	$2.25^{+0.19}_{-0.18}$	$10.5^{+0.98}_{-0.92}$	111.47/103.0
	2	340270285.301	340270285.469	0.168	−3.0	−3.35	1.22	$2.52^{+0.24}_{-0.21}$	$12.54^{+0.86}_{-0.76}$	98.87/96.0
	3	340270409.651	340270410.038	0.387	−0.5	−0.26	1.98	$2.35^{+0.19}_{-0.18}$	$13.28^{+0.54}_{-0.52}$	101.91/96.0
	4	340271426.981	340271427.256	0.275	−4.5	−14.11	0.22	$2.31^{+0.11}_{-0.11}$	$9.96^{+0.31}_{-0.29}$	163.47/152.0
	5	340272005.382	340272005.544	0.162	2.0	−2.3	3.14	$2.47^{+0.11}_{-0.1}$	$12.67^{+0.37}_{-0.35}$	162.76/114.0
	6	340288438.392	340288439.322	0.93	−4.5	−3.53	4.03	$2.25^{+0.18}_{-0.17}$	$11.5^{+0.67}_{-0.62}$	126.45/128.0
	7	340346831.255	340346831.312	0.057	19.5	18.97	1.83	$3.38^{+0.38}_{-0.36}$	$12.07^{+1.28}_{-1.02}$	140.41/107.0
	8	340369053.707	340369054.04	0.333	0.0	−2.21	2.71	$2.5^{+0.16}_{-0.15}$	$8.29^{+0.57}_{-0.56}$	225.8/188.0
	9	340380158.415	340380158.759	0.344	−0.5	−0.87	0.43	$2.38^{+0.09}_{-0.08}$	$11.08^{+0.26}_{-0.25}$	208.5/202.0
	10	340643650.376	340643650.79	0.414	−2.5	−2.94	0.66	$2.26^{+0.08}_{-0.08}$	$8.33^{+0.24}_{-0.23}$	229.45/147.0
	11	341056809.754	341056810.053	0.299	−10.5	−10.21	3.12	$2.44^{+0.16}_{-0.15}$	$8.24^{+0.62}_{-0.55}$	131.33/119.0
	12	341084172.045	341084172.821	0.776	3.5	−2.7	−1.02	$2.38^{+0.15}_{-0.14}$	$8.4^{+0.49}_{-0.46}$	213.16/151.0
Segment 1[b]	13	340260979.802	340260980.05	0.248	−1.0	−1.46	−0.89	$2.15^{+0.17}_{-0.15}$	$11.97^{+0.57}_{-0.52}$	221.68/209.0
	14	340266063.664	340266063.866	0.202	0.0	−0.6	1.59	$2.63^{+0.41}_{-0.35}$	$11.05^{+1.32}_{-1.14}$	69.8/65.0
	15	340270285.301	340270285.365	0.064	−3.0	−3.35	1.22	$2.38^{+0.31}_{-0.28}$	$12.85^{+1.46}_{-1.22}$	60.98/52.0
	16	340270409.651	340270409.75	0.099	−0.5	−0.26	1.98	$2.51^{+0.39}_{-0.35}$	$12.63^{+0.96}_{-0.9}$	89.96/64.0
	17	340271426.981	340271427.079	0.097	−4.5	−14.11	0.22	$2.26^{+0.23}_{-0.21}$	$9.56^{+0.67}_{-0.61}$	101.69/92.0
	18	340272005.382	340272005.413	0.03	2.0	−2.3	3.14	$2.39^{+0.44}_{-0.37}$	$11.32^{+1.09}_{-0.92}$	80.66/58.0
	19	340288438.392	340288438.478	0.086	−4.5	−3.53	4.03	$2.29^{+0.37}_{-0.34}$	$11.17^{+1.07}_{-0.92}$	58.12/55.0
	20	340346831.255	340346831.281	0.026	19.5	18.97	1.83	$3.34^{+0.76}_{-0.6}$	$12.95^{+1.85}_{-1.45}$	84.72/50.0
	21	340369053.707	340369053.855	0.148	0.0	−2.21	2.71	$2.54^{+0.17}_{-0.17}$	$7.42^{+0.62}_{-0.56}$	228.06/203.0
	22	340380158.415	340380158.441	0.025	−0.5	−0.87	0.43	$2.7^{+0.5}_{-0.41}$	$11.38^{+1.1}_{-0.92}$	47.42/51.0
	23	340643650.376	340643650.5	0.124	−2.5	−2.94	0.66	$2.0^{+0.26}_{-0.25}$	$8.82^{+0.73}_{-0.67}$	112.34/97.0
	24	341056809.754	341056809.867	0.113	−10.5	−10.21	3.12	$2.5^{+0.32}_{-0.29}$	$8.59^{+1.29}_{-1.14}$	126.35/105.0
	25	341084172.045	341084172.308	0.263	3.5	−2.7	−1.02	$2.41^{+0.24}_{-0.23}$	$8.25^{+0.73}_{-0.65}$	167.93/125.0
Segment 2[c]	26	340260980.05	340260980.117	0.067	−1.0	−1.46	−0.89	$2.35^{+0.31}_{-0.26}$	$13.08^{+1.68}_{-1.34}$	54.81/42.0
	27	340266063.866	340266064.1	0.234	0.0	−0.6	1.59	$2.02^{+0.16}_{-0.16}$	$10.41^{+1.22}_{-1.07}$	120.95/98.0
	28	340270285.365	340270285.469	0.104	−3.0	−3.35	1.22	$2.62^{+0.36}_{-0.3}$	$12.14^{+1.03}_{-0.89}$	65.77/65.0
	29	340270409.75	340270410.038	0.288	−0.5	−0.26	1.98	$2.46^{+0.26}_{-0.23}$	$13.47^{+0.76}_{-0.71}$	105.25/88.0
	30	340271427.079	340271427.256	0.178	−4.5	−14.11	0.22	$2.48^{+0.31}_{-0.28}$	$10.85^{+0.87}_{-0.77}$	120.71/93.0
	31	340272005.413	340272005.544	0.132	2.0	−2.3	3.14	$2.41^{+0.19}_{-0.17}$	$12.51^{+0.8}_{-0.72}$	128.7/118.0
	32	340281973.549	340281973.9	0.351	0.5	−9.16	7.15	$2.57^{+0.46}_{-0.36}$	$12.4^{+1.52}_{-1.35}$	99.14/80.0
	33	340288438.478	340288439.322	0.844	−4.5	−3.53	4.03	$2.1^{+0.22}_{-0.21}$	$11.41^{+0.82}_{-0.75}$	120.09/106.0
	34	340346831.281	340346831.312	0.031	19.5	18.97	1.83	$3.21^{+0.47}_{-0.41}$	$10.36^{+1.59}_{-1.17}$	84.66/68.0
	35	340369053.855	340369054.04	0.185	0.0	−2.21	2.71	$2.4^{+0.22}_{-0.21}$	$9.45^{+0.83}_{-0.78}$	170.44/147.0
	36	340380158.441	340380158.759	0.318	−0.5	−0.87	0.43	$2.34^{+0.15}_{-0.14}$	$10.9^{+0.49}_{-0.45}$	124.84/110.0
	37	340643650.5	340643650.79	0.29	−2.5	−2.94	0.66	$2.08^{+0.17}_{-0.17}$	$7.42^{+0.48}_{-0.44}$	234.84/198.0
	38	341056809.867	341056810.053	0.186	−10.5	−10.21	3.12	$2.52^{+0.24}_{-0.22}$	$9.36^{+1.11}_{-0.99}$	141.13/134.0
	39	341084172.308	341084172.821	0.513	3.5	−2.7	−1.02	$2.26^{+0.2}_{-0.2}$	$8.36^{+0.63}_{-0.59}$	151.17/155.0

Notes. ts_{lag} is the Monte Carlo simulation result for the original light curve. σ is the simulation sample statistic and fitting result.

[a] For the whole burst spectra.

[b] For the burst rising part or the first main peak from the burst start time to the cut off time, cut off time usually means peak time for single peak burst while valley time for multi-peak burst.

[c] For the burst falling part or the second main peak from the burst cut off time to burst stop time. T_{bb} is the time span of a burst used to do spectra analysis. t_{lag} is the MCCF lag time for a burst in energy band 10–20 keV versus 60–100 keV.

these bursts, we found some special bursts. Their energy spectra cannot be fitted using the traditional magnetar energy spectrum model, such as BB+BB, CPL or BB+PO (blackbody + power-law). They have obvious blackbody characteristics in the low-energy band but strong cut-off power-law spectrum characteristics in the high-energy band.

We carefully studied the energy spectrum of these two strong bursts. We used BB+BB, BB+PO, BB+CPL, CPL, and CPL +Gaussian models to fit the energy spectrum of the burst triggered at October 2022 18T00:29:36.895. The BB+PO model was excluded due to poor fitting goodness. When using the BB+CPL model for fitting, if the model parameters are
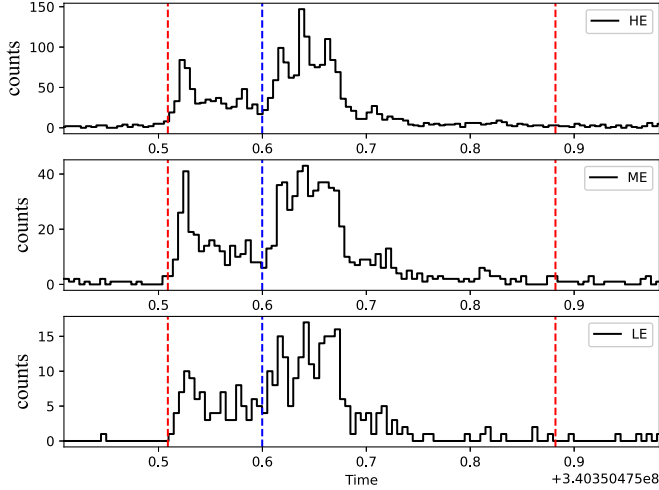
Figure 5. The schematic diagram of the time decomposition points of multi-peak burst. The two red vertical dashed lines represent the beginning and end moments of the burst, respectively, while the blue dashed line represents the decomposition time point. The interval between the left red line and the blue line is designated as segment 1, whereas the duration between the blue line and the second red line is categorized as segment 2.
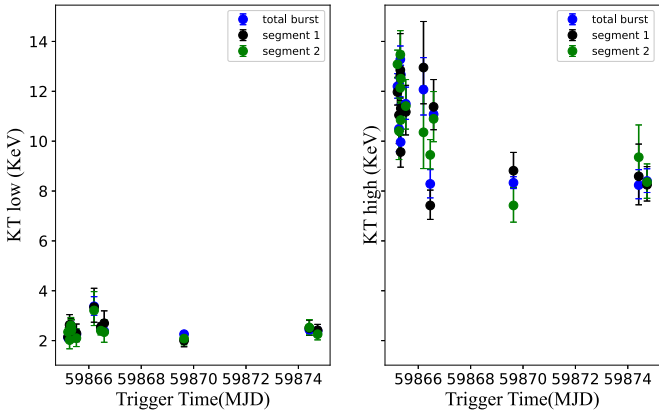

Figure 6. Blackbody temperature distribution of time-resolved spectra. The left panel is for the low temperature distribution of the BB+BB bursts, while the right panel is for the high temperature. In both panels, the blue dot is the parameter for the total burst, the black dot is for segment 1, and the green dot is for segment 2.

allowed to change freely, the CPL index factor obtained by fitting is very small, on the order of 10^3, which is too different from the index factors in all magnetar bursts of the same type. So we first use the CPL model to fit the exponential factor, fix the factor, and then add the BB model. No matter which model among BB+BB, BB+CPL and CPL is used, there is still a peak structure near 7 keV in the residual plot, and the goodness of fit is poor. The null hypothesis probability value of the chi-square test is very small. But when using the CPL+Gaussian model, we obtained the best-fitting goodness and the smallest

residual. The line center energy obtained by fitting is about 6.78 keV, and the sigma is 1.97 keV. We chose the F-test to find that the significant advantage of this model compared to other models is about 3σ. We also conducted a time decomposition spectrum study for the burst and found that the line feature almost disappeared during the rising time period, but existed during the peak time period and falling time period, which shows that this line feature does not exist within the time range of the entire burst, but only appears in specific parts. It is worth noting that, in our analysis, we fixed the interstellar absorption factor NH at 2.79, which was determined based on the fitting results of other bursts exhibiting significant spectral characteristics. Relaxing this parameter had no impact on the aforementioned conclusion. Another burst triggered at October 2022 14T05:47:52.515 also has this spectrum characteristic. The obtained line center energy is consistent with the first one. The difference is that the BB+CPL model for this burst also can obtain the same goodness as Gaussian+CPL with the BB temperature 2.1 keV. In summary, the analysis results show that this emission line may exist, and may only exist in a part of the burst. The spectra for the two bursts is shown in Figures 7 and 8. It can be seen from the residual plot that only low-energy blackbody (or line) and high-energy CPL can fit the energy spectrum properly.

5. Discussion

In this study, we found that the burst photon distribution presents a three-peak structure, and the peak position is not aligned with the persistent radiation profile, and the burst number is most near the secondary peak of persistent radiation. If the persistent radiation is assumed to be related to the geometry of the magnetic field, then the distribution of the burst events suggests that there may be some intrinsic relationship between the bursts and the geometry of the magnetic field. We simply analyze the bursts on both sides of the main peak of persistent radiation, and only select partial bursts with higher intensity. The preliminary analysis results show that there is a significant difference in the power index factor of the CPL spectrum on the two sides, which indicates that the distribution index of electrons producing energy truncation is different. If the relationship between the observation line of sight and the direction of the rotation axis and the magnetic pole is considered, the above results show that the distribution of electrons (or positrons) is related to the direction of the magnetic field. The time-resolved spectral analysis result shows that the spectral parameters have uniform invariance at any time of the burst, which indicates that the environment in our observation path is relatively stable during a burst duration. For the CPL spectrum, that is, the electron distribution passed by the radiation seed photon before reaching the observer is stable. In fact, the electrons present in the strong magnetic field are rapidly dissipated by the
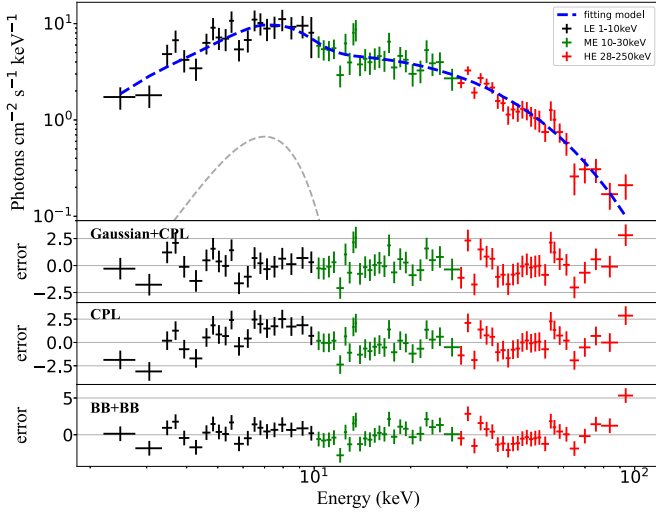
Figure 7. The burst spectrum triggered at October 2022 18T00:29:36.895 UTC. The top panel shows the raw data and the Gaussian+CPL model results. The left panels show the residuals of Gaussian+CPL, CPL, and BB+BB, respectively. The dark gray dashed line in the top panel shows the Gaussian model.
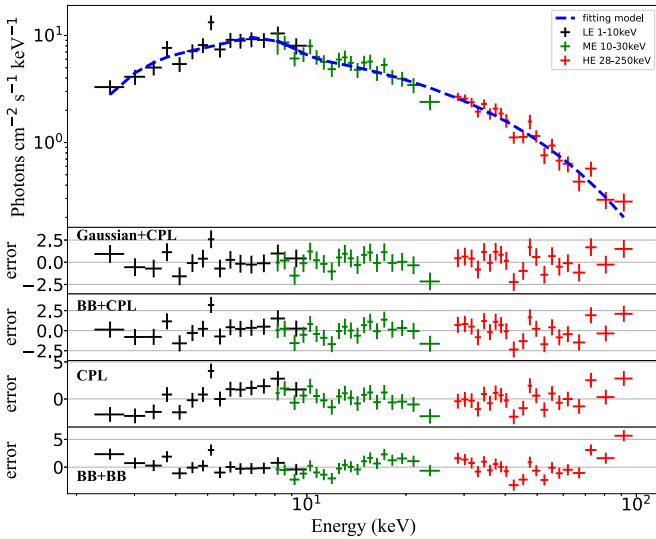

Figure 8. The burst spectrum triggered at October 2022 14T05:47:52.515 UTC. The top panel shows the raw data and the BB+CPL model results. The left panels show the residuals of Gaussian+CPL, BB+CPL, CPL, and BB +BB, respectively.

synchrotron radiation attenuation, so the stable process that we observe suggests that there is a very stable continuous process that is constantly producing and replenishing electrons with stable energy. Thus we can infer that the large magnetic field environment is relatively stable, which supports the magnetic field structure theory that the magnetic field of magnetars is dominated by a stable dipole field.

We also found that some burst spectra have the form of blackbody plus CPL, and the blackbody temperature is the same as that of the low-temperature blackbody of the double blackbody burst. This new spectrum model reminds us that the blackbody spectrum may be the most basic spectrum type in the magnetar burst, that is, the burst generated at the beginning is a blackbody, but in the radiation emission process, because of the encounter of electron clumps, The interaction between the two changes the shape of the energy spectrum, due to the different distribution of electrons, the amount of change is different. When the change is thorough, the energy spectrum is directly power-scaled. When the change is partial, the energy spectrum will retain the blackbody component.

The appearance of Gaussian plus CPL spectral type indicates the possibility of an emission line. According to the current magnetar models, this emission line is not expected. If there is an emission line reflected by an accretion disk, the emission line should exist at all times in all bursts, contradicting the observational results. Therefore, if this emission line exists, a new mechanism is needed. For example, in the model of an asteroid impacting a magnetar reported in Dai (2020) for the FRB, there should be moving asteroids around the magnetar, so it is possible that reflections from the asteroids could produce iron emission lines. Due to the randomness of the location and time of asteroid appearance, the occasional emission lines can be explained. However, this assumption needs to be confirmed carefully by future observations.

ORCID iDs

Xue-Feng Lu ⓘ https://orcid.org/0000-0003-1272-3997
Li-Ming Song ⓘ https://orcid.org/0000-0003-0274-3396

References

Buccheri, R., Bennett, K., Bignami, G. F., et al. 1983, A&A, 128, 245
Cai, C., Xiong, S.-L., Lin, L., et al. 2022a, ApJS, 260, 25
Cai, C., Xue, W.-C., Li, C.-K., et al. 2022b, ApJS, 260, 24
Cao, X., Jiang, W., Meng, B., et al. 2020, SCPMA, 63, 249504
Chen, Y., Cui, W., Li, W., et al. 2020, SCPMA, 63, 249505
Dai, Z. G. 2020, ApJL, 897, L40
Dong, F. A. & Chime/Frb Collaboration 2022, ATel, 15681, 1
Enoto, T., Hu, C.-P., Guver, T., et al. 2022, ATel, 15690, 1
Frederiks, D., Ridnaia, A., Svinkin, D., et al. 2022, ATel, 15686, 1
Ge, M.-Y., Yang, Y.-P., Lu, F.-J., et al. 2024, RAA, 24, 015016

Huang, Y. X., Xu, H., Xu, Y. H., et al. 2022, ATel, 15707, 1
Israel, G. L., Esposito, P., Rea, N., et al. 2016, MNRAS, 457, 3448
Kaspi, V. M., & Beloborodov, A. M. 2017, ARA&A, 55, 261
Kothes, R., Sun, X., Gaensler, B., & Reich, W. 2018, ApJ, 852, 54
Kouveliotou, C., Dieters, S., Strohmayer, T., et al. 1998, Natur, 393, 235
Li, T. 2004, ChJAA, 4, 583
Li, X. B., Zhang, S. N., Xiong, S. L., et al. 2022, ATel, 15708, 1
Lin, L., Göğüş, E., Roberts, O. J., et al. 2020, ApJ, 893, 156
Liu, C., Zhang, Y., Li, X., et al. 2020, SCPMA, 63, 249503
Lu, X.-F., Song, L.-M., Ge, M.-Y., et al. 2023, RAA, 23, 035007
Maan, Y., Leeuwen, J. v., Straal, S., & Pastor-Marazuela, I. 2022, ATel, 15697, 1
Palm, D. M. 2022, ATel, 15667, 1

Roberts, O. J., Dalessi, S., & Malacaria, C. 2022, ATel, 15672, 1
Scargle, J. D., Norris, J. P., Jackson, B., & Chiang, J. 2013, ApJ, 764, 167
Scholz, P., & Kaspi, V. 2011, ApJ, 739, 94
Stamatikos, M., Malesani, D., Page, K. L., & Sakamoto, T. 2014, GCN, 16520, 1
Thompson, C., & Duncan, R. C. 1995, MNRAS, 275, 255
Wang, C. W., Xiong, S. L., Zhang, Y. Q., et al. 2022, ATel, 15682, 1
Woods, P., Kouveliotou, C., Gavriil, F., et al. 2008, ApJ, 629, 985
Xiao, S., Tuo, Y.-L., Zhang, S.-N., et al. 2023, MNRAS, 521, 5308
Younes, G., Enoto, T., Hu, C.-P., et al. 2022, ATel, 15674, 1
Younes, G., Güver, T., Kouveliotou, C., et al. 2020, ApJL, 904, L21
Younes, G., Kouveliotou, C., Van der Horst, A. J., et al. 2017, ApJ, 847, 85
Zhang, S.-N., Li, T., Lu, F., et al. 2020, SCPMA, 63, 249502